Chemosphere 278 (2021) 130239

Contents lists available at ScienceDirect

Chemosphere

journal homepage: www.elsevier.com/locate/chemosphere

Process optimization for the synthesis of ceramsites in terms of mechanical strength and phosphate adsorption capacity

Jui-Yen Lin [a], Dan Li [b], Minsoo Kim [b], Ingyu Lee [b], Hyunook Kim [b, *], Chin-Pao Huang [a, **]

[a] Department of Civil and Environmental Engineering, University of Delaware, Newark, DE, 19716, United States
[b] Department of Environmental Engineering, University of Seoul, Seoul, 02504, South Korea

HIGHLIGHTS

- Ceramsites were synthesized from thermal treatment of red mud, successfully.
- 64 wt% of KRRM at 1000 °C produced the best performing ceramsites.
- 48 wt% of USRM at 700 °C produced the best performing ceramsites.
- Best performing ceramsites exhibited high adsorption capacity and mechanical strength.
- Kinetic and isotherms of phosphate adsorption were studied.

ARTICLE INFO

Article history:
Received 17 December 2020
Received in revised form
8 February 2021
Accepted 5 March 2021
Available online 23 March 2021

Handling Editor: Y Yeomin Yoon

Keywords:
Ceramsites
Granulation
Compression stress
Phosphate adsorption capacity
Process optimization

ABSTRACT

Red mud (RM), an industrial waste of bauxite refinery, shows great potential in adsorptive phosphate immobilization but granulation of RM enables the ease for field application. Red-mud-based ceramsites with 12 compositions that blended Korean red mud, American red mud, ocher, and bentonite were synthesized through firing process (600–1000 °C). The porosity, bulk density, mechanical strength, mineralogical composition, and phosphate adsorption capacity of granulated RM were characterized and analyzed. The crystallization of plagioclases, nepheline and gehlenite was observed in the ceramsites with high alkali flux content, which enhanced both porosity and phosphate adsorption capacity. The characteristics of the ceramsites without phase transition were highly correlated with porosity. The mechanical strength of ceramsites was governed by crack population, describable by the Weibull distribution model, and thus the maximal tensile stress correlated negatively with porosity. Results showed that 32 wt % of KRREM and USREM treated at 1000 and 900 °C, respectively, yielded the best performing ceramites in terms of mechanical strength and phosphate adsorption capacity. Ultimately, the phosphate adsorption capacity, as affected by initial phosphate concentration, contact time, and temperature, of the optimized ceramsites was studied.

1. Introduction

Phosphate is a limiting nutrient for phytoplankton growth. Ineffective phosphate control would cause eutrophication and phytoplankton bloom in the natural water system, which deteriorates water quality and endangers aquatic ecosystem (Li et al., 2016). Adsorption is an attractive process for phosphate removal from dilute streams due to high removal efficiency, cost-effective, and simple operation (Huang et al., 2017). A variety of soils, clays, and mineral oxides have been reported to have significant adsorption capacity toward phosphate (Gérard, 2016; Li et al., 2016). The possibility of utilizing mineral processing wastes, such as fly ash, furnace slag, and biosolids as low-cost adsorbents has been extensively explored (Jellali et al., 2011; Ge et al., 2018; Yasipourtehrani et al., 2019).

Red mud (RM), commonly known as bauxite residue, is the insoluble fine material during caustic digestion of bauxite in alumina refining process. The production of red mud was estimated at 3 billion tons in 2010 or an average of 140 million tons per year worldwide (International Aluminium Institute, 2015). High in iron

* Corresponding author.
** Corresponding author.
E-mail addresses: jylin@udel.edu (J.-Y. Lin), iicegrad201528@uos.ac.kr (D. Li), powerhead12@uos.ac.kr (M. Kim), ingyu@uos.ac.kr (I. Lee), h_kim@uos.ac.kr (H. Kim), huang@udel.edu (C.-P. Huang).

https://doi.org/10.1016/j.chemosphere.2021.130239
0045-6535/

and aluminum oxide content renders RM effective in removing toxic chemicals from aqueous solutions (Bhatnagar et al., 2011). Specifically, RM can be fabricated as granules and used as the substrate of constructed wetlands to improve the removal of micronutrients, namely, phsphorus. In this case, the red mud-based granular adsorbents should meet the requirement of mechanical strength and chemical stability (Wu et al., 2015). Zhu et al. (2007) first synthesized a granular red-mud-based adsorbent for cadmium removal. The raw materials, including red mud, fly ash, sodium carbonate, quick lime, and sodium silicate, were calcination at 400 and 800 °C. Tor et al. (2009) applied the same granular adsorbents for defluorination. Several investigators conducted a series of studies to synthesize granular adsorbents by sintering red mud with starch and bentonite as binders at 1000 °C (Yue et al., 2010; Zhao et al., 2010, 2012a, 2012b). The produced adsorbents showed certain affinity toward phosphate adsorption at a capacity of 6.64 mg-P g^{-1} and the spent granulized red mud could be regenerated using dilute HCl or NaOH. In addition to sintering, Ye et al. (2015) prepared RM granules using carboxyl cellulose as a gelling agent to bound RM powders with straw at 200 °C. The red mud granules had high specific surface area (113.5 m^2 g^{-1}) and phosphate adsorption capacity (86.69 mg-P g^{-1}). However, RM with organic binding may suffer from biodegradation in long-term operation.

Synthesizing RM-based granules through firing resembles the preparation of ceramsite and aggregate in process. Many studies have utilized waste materials, such as fly ash, wastewater sludge, waste glass, and oyster shell as raw material for the preparation of ceramsites with high mechanical strength (Yang et al., 2013; Wei et al., 2017; Lu et al., 2013; Wei and Ko, 2017). The parameters in the ceramsite synthesis include particle size and mass fraction of raw materials, methods, and the temperature and time during preheating and final calcination among others. Among the above parameters, calcination temperature and mass ratio of raw materials were key factors for the synthesis of ceramsites (Cheng et al., 2018; Liu et al., 2017; Zou et al., 2009). For water and wastewater treatment applications, the adsorption capacity of ceramsite is as important as its mechanical strength. Intuitively, vitrification reaction tends to enhance the mechanical strength, it also would reduce the specific surface area thus minimizing the available active site for adsorption. Therefore, it is important to establish synthesis process for optimizing the mechanical strength and adsorption capacity of ceramsites simultaneously. To the best of our knowledge, past research focused more on the adsorption performance only than combined mechanical strength and adsorption capacity consideration in the preparation of RM adsorbents. Cheng et al. (2018) and Zou et al. (2009) were among the first to suggest that ceramsites for water quality control should consider low bulk density, high engineering strength, and high adsorption capacity.

The objective of this study was to optimize the chemical composition and sintering temperature for the preparation of ceramsites from RM toward high phosphate adsorption capacity and mechanical strength. As the physical-chemical characteristics of RM was dependent on the source of bauxite and refining process, two varieties of red mud, namely, Korean red mud (KRRM) and American red mud (USRM), were selected as the raw materials in this study due to their distinct mineral composition and properties. In addition, various amounts of Korean ocher (OCHR) and bentonite (BENT) were blended with RM to prepare granular RM adsorbents. The apparent porosity, mechanical strength, phosphate adsorption capacity and mineralogical composition of the ceramsites were characterized and analyzed statistically. Ultimately, an optimal process was established for ceramsites preparation toward high phosphate adsorption capacity and mechanical strength.

2. Materials and methods

2.1. Materials

Two types of RM were used in this research, including American red mud (USRM), supplied by Noranda Alumina in Gramercy, LA, USA, and Korean red mud (KRRM), supplied by Cheong-Ho Environment Development Co., Ltd., South Korea. Cheong-Ho Environment Development Co. also supplied silica-rich ocher (OCHR). Bentonite (BENT) (sodium form) was purchased from Fisher Scientific, OCHR and BENT were used as amendments for binding and for increasing the plasticity for molding, respectively. All materials were ground using burr-type coffee grinder (DBM-8 Supreme, Cuisinart, CT, USA) and sieved through 60 mesh (250 μm). The sieved samples were dried at 105 °C overnight and stored in a desiccator before use.

The fluorite used in quantitative X-ray diffraction was purchased from Alfa Aesar (CaF_2, >99.5%) and the particle size was finer than 325 mesh. Sodium chloride (NaCl) and monosodium phosphate monohydrate ($NaH_2PO_4 \cdot H_2O$) were purchased from Alfa Aesar, Tewksbury, MA, USA.

2.2. Preparation of ceramsites

KRRM-based and USRM-based ceramsites were prepared from KRRM and USRM, respectively, using OCHR and BENT as binder and plasticizer, respectively. The fraction of BENT was kept constant at 20 wt% to provide constant plasticity, whereas the rest of 80 wt% was the mixture of RM and OCHR; the fraction of RM was 0, 16, 32, 48, 64, and 80 wt%. Figure S1 presents the flow chart of ceramiste preparation. The mixture, 60 g of materials at specific fraction of RM, BENT, and OCHR in a 125 mL PE bottle, was homogenized by mixing rotationally at 30 rpm for 2 h. The powder was first moisturized by adding deionized water at water content of 34 ± 2 wt% on a wet weight basis. The paste was molded into a spherical shape with a diameter of 1 cm using round bullet molds (Lee.310" round bullet mold, Track of the Wolf Inc., Elk River, MN, USA). The damp granules were dried at 50 °C and a relative humidity of 75% (controlled by saturated sodium chloride solution according to ASTM E104-02 (ASTM, 2012)) in a closed chamber (V = 5600 cm^3, A = 1260 cm^2, Rubbermaid, GA, USA) for 72 h. The dried granules were sintered at 600–1000 °C with an interval of 100 °C for 1 h with a ramping rate of 5 °C•min^{-1}. The fired granules were neutralized in 10^{-2} M HCl for 2 h twice and in deionized water for 20 min thrice at solid to liquid ratio of 100 g-L^{-1} as to reduce the alkalinity. Afterwards, the neutralized granules were dried at 105 °C overnight and stored in a desiccator before further evaluation.

2.3. Characterization

The chemical composition of all raw materials (KRRM, USRM, OCHR, and BENT) was quantified using X-ray fluorescence (XRF, Supermini 200, Rigaku Co., Austin, TX, USA) under helium atmosphere. The mineralogical composition was characterized using an X-ray diffractometry (XRD, Bruker D8 Discover, Bruker AXS Inc., Madison, WI, USA) equipped with a LynxEyeXE detector. The wavelength of X-ray was 1.54 Å, generated by Cu Kα radiation (40 kV, 40 mA) and filtered by a Nickel filter. The samples were downsized to <44 μm (325 mesh) and mixed with 15.0 wt% of fluorite (Alfa Aesar, CaF_2, >99.5%) for phase quantification. The scanning degree started from 20° to 90°, with an increment of 0.05° and scanning time of 0.5 s. The diffraction pattern was analyzed according to the Rietveld method using Profex 3.14.0 for quantification (Doebelin and Kleeberg, 2015; Zhou et al., 2018). The specific surface area and pore volume of the raw material were measured

by Micromertics ASAP 2020 (Micrometrics Instrument Co., Norcross, GA, USA). The hysteresis loop of N_2(g) adsorption and desorption was acquired at 77.54 K. TGA/DSC (SDT Q600, TA Instrument, New Castle, DE, USA) was to study the reactions involving RMs, OCHR, BENT, and their mixture while being fired at a ramping rate of 20 °C- min^{-1} under air atmosphere at flow rate of 50 mL-min^{-1}. At least 10 mg of the sample was used in each analysis.

The apparent porosity of the ceramsite was evaluated according to ASTM methods (ASTM, 2015, 2016). The ceramsites were boiled in DI water for 2 h and kept immersed for at least 12 h for complete saturation. The saturated weight (W, g) and suspended weight (S, g) of the specimen were determined using a density balance (AT 200, Mettler Toledo, Columbus, OH, USA). The dry weight (D, g) was determined after drying at 105 °C for 12 h. The bulk volume (V, cm^3), apparent porosity (ϕ), and bulk density (ρ_b) of the specimen were calculated.

$$V = \frac{W - S}{\rho_w} \tag{1}$$

$$\phi = \frac{W - D}{V} \times 100\% \tag{2}$$

$$\rho_b = \frac{D}{V} = \frac{D}{W - S} \tag{3}$$

where ρ_w is water density (g-cm^{-3}). The mechanical strength of the ceramsite was evaluated by compression test using a universal testing system (Model 5567, Instron, Norwood, MA, USA) coupled with a 5 kN load cell. The displacement rate was 0.127 cm-min^{-1} and the maximal applied force at failure was recorded. At least 10 specimens were tested for every sample to statistically analyze the failure probability according to the Weibull distribution, which expresses the failing probability as a function of applied stress.

$$P_f = 1 - \exp\left[- \left(\frac{\sigma}{\sigma_\theta} \right)^m \right] \tag{4}$$

$$P_{f,i} = \frac{i - 0.5}{N} \tag{5}$$

where P_f is the probability of failure, m is the Weibull modulus, σ is the tensile stress (MPa), and σ_θ is the Weibull characteristic strength (MPa), which is dependent on the size and geometry of the specimen, N is the number of specimens, and i denotes the ith datum. The Weibull modulus and the Weibull characteristic strength were obtained by linearizing Eq. (4) through double logarithm. The Hiramatsu and Oka's approximation, as shown in Eq. (6), were used to estimate the tensile stress (σ) of the spherical granule during compression between two plates (Hiramatsu and Oka, 1966; Pejchal et al., 2017).

$$\sigma = 1.4 \times \frac{F}{\pi R^2} \tag{6a}$$

where F is the peak (failure) load and R is the radius of the testing specimen.

2.4. Adsorption experiments

The phosphate solution containing 78 mg-P L^{-1} (2.4×10^{-3} M) and 10^{-2} M NaCl as ionic strength. Thirty mL of phosphate solution and 1 g of ceramsite were mixed in a 50-mL LDPE tube, yielding a solid to liquid ratio of 20 ± 2 g/L. The reaction pH was controlled at 6.8 ± 0.2 using 0.2 M HCl and NaOH. The suspensions were agitated on an orbital shaker at 100 rpm under ambient condition for 48 h. The sample was filtered through a nylon membrane filter with a pore size of 0.45 μm (Simsii Inc., Irvine, CA, USA). The residual phosphate concentration in the filtrate was determined by the vanadomolybdo phosphoric acid colorimetric method, i.e., the yellow method. A spectrophotometer (UV1280, Shimadzu, Kyoto, Japan) was used to measure the absorbance of the sample at 430 nm.

To study the kinetics of phosphate adsorption by the optimized ceramsites, six pieces of ceramsites were placed in 250 mL Erlenmeyer flask containing 200 mL of solution containing an initial phosphate concentration of 10–150 ppm-P and 10 mM of NaCl to reach the solid-to-liquid ratio of 16 g/L and 20 g/L of KRRM-based and USRM-based ceramsites, respectively. The flasks were shaken on an orbital shaker at 100 rpm and 20 °C with pH being controlled at 6.8 ± 0.2. At specific time intervals, one-mL aliquot was sampled and analyzed for residual phosphate concentration as discussed above. To study the equilibrium adsorption, the optimized ceramsites sample was ground with a mortar and pestle until finer than 250 μm (60 mesh). The ground ceramsites were equilibrated with phosphate containing solution (initial concentrations of 10–180 ppm-P in 10 mM NaCl at solid-to-liquid ratio of 4 g/L) under constant shaking at 10, 20 and 30 °C in an environmental room for 4 days, while the pH value was being controlled at 6.8 ± 0.2.

3. Results and discussion

3.1. Raw material characteristics

3.1.1. Chemical and mineralogical composition

Fig. 1 presents the chemical and mineralogical compositions of all raw materials used, including KRRM, USRM, OCHR, and BENT. Table S1 gives the XRD standards for the identification of related crystalline phases. The high Fe_2O_3 content of USRM agreed with that of typical bauxite residues produced *via* the Bayer process (Liu et al, 2011, 2013). In addition to hematite, minor crystalline calcite and sodium oxide (<5 wt%) were observed in USRM, accompanied by 51.3 wt% of amorphous materials. The composition of KRRM deviated from that of reported RM, which might be attributed to the distinctive bauxite origin and refining process. More than 68 wt % of KRRM were amorphous and the richest components were Na_2O (26.3 wt%) and Al_2O_3 (21.4 wt%). Korean ocher and BENT shared similar chemical composition, 60 wt% SiO_2 and 25 wt% Al_2O_3, but their mineralogical contents were completely different. Korean ocher comprised of 51 wt% of quartz, while BENT was mostly in forms of bentonite and cristobalite.

3.1.2. Particle size distribution

Figure S3 and Table S2 show the cumulative volume size distribution and particle size of KRRM, USRM, OCHR, and BENT. Among four ingredients, KRRM was the finest material with d_{50} of 1.6 μm and the lowest uniformity coefficient (4.5), which suggested that the size distribution was narrow. The d_{50} of BENT was 11.3 μm with a uniformity coefficient of 7.9. On the other hand, USRM and OCHR were much coarser, with d_{50} of 59.2 and 72.1 μm, respectively. The uniformity coefficient greater than 15, namely, 15.8 for OCHR and 22.7 for USRM, indicated highly-dispersed nature of the particle size distribution in USRM and OCHR. Figure S4 presents the deconvoluted size distribution of the raw materials as the combination of several log-normal distributions. The distinctive size

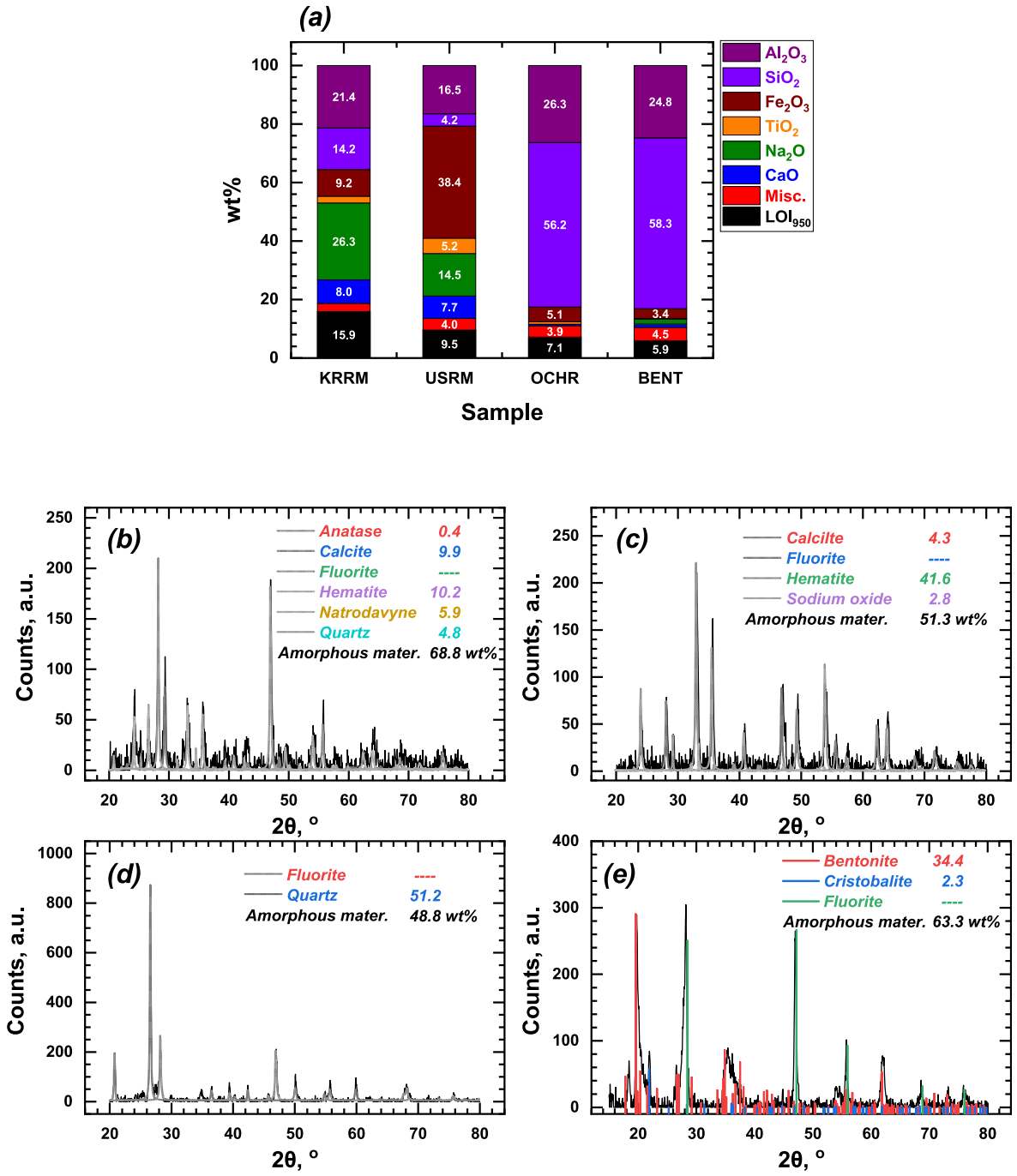

Fig. 1. (a) Chemical composition of KRRM, USRM, OCHR, and BENT as metal oxide and quantitative XRD of (b) KRRM, (c) USRM, (d) OCHR, and (e) BENT (Refer to Table 1 for diffraction standards.).

distribution of RMs was attributed to differences in sources and preparation processes of bauxite. The mineral grains insoluble in the caustic digestant became large particles while some small nuclei were produced during the dissolution-precipitation route (Hind et al., 1999). Table S3 summarizes the geometric mean and volume percent of KRRM, USRM, OCHR and BENT, respectively.

3.1.3. Thermal analysis

The thermogravimetry (TG), derivative thermogravimetry (DTG), and differential thermal analysis (DTA) of KRRM, USRM, OCHR, and BENT are shown in Fig. 2. In general, the events that involve weight loss are dehydration of surface and structured water, combustion or pyrolysis of organic compounds, dehydroxylation and decarbonatization (Plante et al., 2009; He et al., 2012). The above reactions are all endothermic except for the combustion of organics in oxidative atmosphere, which is exothermic. Reactions without weight change can only be revealed in DTA. Endothermic reactions without weight change may be structure transformation, magnetic change, sintering and melting. Exothermic reactions can be iron oxidation and crystallization of amorphous materials (Plante et al., 2009).

Fig. 2a displays the thermogram of KRRM, revealing several

Table 1
Correlation analysis of KRRM-based ceramsites.

KRRM-based ceramsites without phase transition										
		ϕ	Γ	σ	Bentonite	Calcite	Hematite	Natrodavyne	Quartz	Amorphous
ϕ	Pearson'r	1	.746[b]	-.930[b]	-.204	.644[b]	.875[b]	.735[b]	-.876[b]	.441
	p-value		.000	.000	.389	.002	.000	.000	.000	.052
	N	20	20	20	20	20	20	20	20	20
Γ	Pearson'r	.746[b]	1	-.758[b]	-.058	.505[c]	.530[c]	.612[b]	-.630[b]	.320
	p-value	.000		.000	.808	.023	.016	.004	.003	.169
	N	20	20	20	20	20	20	20	20	20
σ	Pearson'r	-.930[b]	-.758[b]	1	-.075	-.631[b]	-.730[b]	-.648[b]	.727[b]	-.220
	p-value	.000	.000		.752	.003	.000	.002	.000	.351
	N	20	20	20	20	20	20	20	20	20

KRRM-based ceramsites with phase transition											
		ϕ	Γ	σ	Hematite	Quartz	Amorphous	Plagiaclases	Ghelenite	Nepheline	New phases[a]
ϕ	Pearson'r	1	.728	-.993[b]	.985[b]	-.841[c]	-.463	-.877[b]	.721	.915[b]	.673
	p-value		.063	.000	.000	.018	.295	.010	.068	.004	.098
	N	7	7	7	7	7	7	7	7	7	7
Γ	Pearson'r	.728	1	-.669	.697	-.794[c]	-.595	-.536	.787[c]	.799[c]	.907[b]
	p-value	.063		.100	.082	.033	.159	.215	.036	.031	.005
	N	7	7	7	7	7	7	7	7	7	7
σ	Pearson'r	-.993[b]	-.669	1	-.977[b]	.781[c]	.473	.858[c]	-.683	-.876[b]	-.621
	p-value	.000	.100		.000	.038	.283	.013	.091	.010	.137
	N	7	7	7	7	7	7	7	7	7	7

[a] New phases equals to the sum of plagioclases, ghelenite and nepheline.
[b] Correlation is significant at the 0.01 level (2-tailed).
[c] Correlation is significant at the 0.05 level (2-tailed).

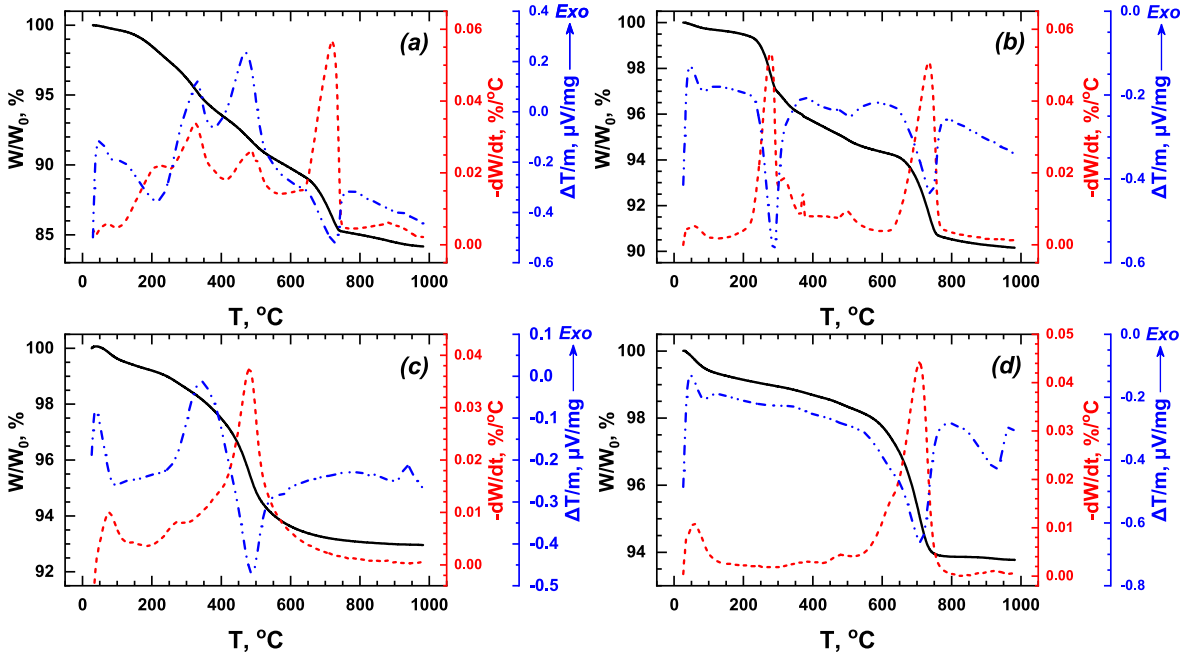

Fig. 2. TG (solid line), DTG (dashed line) and DTA (dashed-dotted line) thermograms of (a) KRRM, (b) USRM, (c) OCHR and (d) BENT. (Ramping rate = 20 °C min^{-1}, purging gas = 50 mL-air min^{-1}).

weight loss and endo/exothermal events. The endothermic reaction involving weight loss below 250 °C was attributed to the removal of water *via* evaporation, including surface water and crystalline water (Girgis et al., 1987). Two weight loss events coupled with significant exothermic signals at 320 °C and 480 °C suggested that KRRM had high organic compounds and distinctive thermal stability. The low-temperature event was attributed to dehydration and decarboxylation of surface carboxyl group, whereas the high-temperature event was caused by decomposition of aromatics in humic substances (Provenzano and Senesi, 1999). At 720 °C, the endothermic weight loss was contributed by the decomposition of carbonate-containing minerals, including calcite and natrodavyne (Buhl, 1991; Radha et al., 2010). Beyond 700 °C, although no apparent weight loss or exo/endotherms was observed, the changed slope with respect to the base line suggested that partial melting of fluxes, such as Na_2O and CaO, might take place that altered the heat capacity. Fig. 2b shows that the reactions of USRM were all endothermic, indicating that there were little organic compounds in USRM. The weight losses between 200 °C and 600 °C were contributed by the dehydration and dehydroxylation of

residual bauxite minerals. Gibbsite dehydrated at 280 °C; diaspore and boehmite dehydroxylate at 315 °C and near 500 °C, respectively (Kloprogge et al., 2002). The intense endothermic weight loss at 730 °C was ascribable to decarbonatization of calcite (Radha et al., 2010). It is expected that other surface analyses such as FTIR and XPS will be useful to study surface reactions such as dehydration, organic burnout, decarbonization, and dehydroxylation on red muds, owing to the change in the stretching of the chemical bounds and the bonding energy of the elements, as well (Kloprogge et al., 2002; Hu et al., 2019). Fig. 2c shows the thermogram of OCHR. The broad exothermic band at 350 °C revealed that OCHR contained organic compounds with various degrees of thermal stability. The weight loss of 2.8 wt% at 490 °C was likely due to the dehydroxylation of boehmite (Kloprogge et al., 2002), suggesting that amorphous boehmite might make up 16 wt% of OCHR. The exotherm without weight loss at 937 °C was contributed by the crystallization of amorphous quartz (shown later). Fig. 2d displays the thermal analysis of BENT. Apart from the removal of surface water below 150 °C, the endotherms at 700 °C and 930 °C were contributed by the dehydroxylation of bentonite and the breakdown of montmorillonite structure, individually (Stanković et al., 2011; Wolters and Emmerich, 2007).

3.2. Characteristics of synthesized ceramsites

3.2.1. Thermal and mineralogical analysis

Figure S4 shows the chemical composition of 12 granules prepared from RM, OCHR, and BENT at different OCHR to RM weight ratios and constant 20% BENT weight fraction. Several ceramsites sintered at 600 °C showed low integrity and disintegrated during neutralization process, including the ones prepared with 16, 32, and 48 wt% of KRRM and 48, 64, and 80 wt% of USRM. Fig. 3 presents the thermogram of KRRM-based and USRM-based granules in airflow from 50 to 1000 °C. Since the reactions below 800 °C were dehydration, dehydroxylation, organic combustion, and decarbonatization, the intensities of the thermal events were the summation of the above four reactions at specific weight ratio or raw materials. For example, the differential weight loss and endothermic energy of decarbonatization at 700 °C increased with the weight fraction of RM. On the other hand, the exotherms occurred at T > 800 °C did not follow the weight ratio. The blend without RM exhibited an exothermic band at 935 °C, which was contributed by OCHR. For USRM-based blends, the exotherm faded as the fraction of OCHR decreased and could no longer be observed when the fraction of USRM was greater than 32 wt%. However, the case of KRRM-based blends showed differently from those of the USRM-based. As the fraction of KRRM increased, the exotherm not only intensified but also shifted downwards from 935 °C to 892 °C, which phase transition upon the introduction of KRRM.

In order to verify the formation of KRRM-based ceramsites, quantitative XRD was conducted according to Rietveld refinement (Rietveld, 1969) as shown in Fig. 4. The phases observed in ceramsites with KRRM ≤16 wt% were bentonite and quartz, while the content of the latter increased with temperature, suggesting the crystallization of amorphous silicon dioxide. As the content of KRRM increased, the fraction of alkali flux components (i.e., Na_2O and CaO) increased, which enhanced the liquidation upon firing and promoted the formation of new phases at T > 900 °C. The plagioclases, a series of minerals, composed of different fraction of albite ($NaAlSi_3O_8$) and anorthite ($CaAl_2Si_2O_8$), were observed when the KRRM content was between 32 and 64 wt%, while nepheline ($NaAlSiO_4$) and gehlenite ($Ca_2Al_2SiO_7$) were formed when the KRRM content was greater than 64 and 80 wt%, respectively. Meanwhile, the content of amorphous materials decreased significantly. The alkali flux, originated from the decomposition of calcite ($CaCO_3$) and natrodavyne ($Na_3Al_3SiO_{12}\cdot Na_2CO_3$), led to partial melting in the inner surface and cracks of the ceramsites where the plagioclases nucleated and grew (Johannes et al., 1994). As the fraction of KRRM increased, the content of Na_2O increased so that the fluid-mediated dissolution-reprecipitation reaction enabled the exchange reaction between Na^+ and Ca^{2+} to form nepheline from albitic plagioclases (Upadhyay, 2012). The crystallization of nepheline increased CaO content in the liquid phase and, therefore, triggered the secondary crystallization flossrom nepheline to gehlenite at the surface of the grain (Nowok et al., 1990). As will be shown later, the KRRM-based ceramsites will have much smaller specific surface area than that of raw materials due to the vitrification process. Our previous results also revealed that the morphology of KRRM was smoothened and its pH_{pzc} was decreased with the activation temperature (Lin et al., 2020). In contrast, the crystalline substances in the USRM-based ceramsites included only quartz, bentonite, calcite, and hematite regardless of sintering temperature (not shown), suggesting the absence of phase transformation.

3.2.2. Porosity, mechanical strength and adsorption capacity

Fig. 5 presents characteristics of ceramsites, including apparent porosity (ϕ), mechanical strength (σ) and phosphate adsorption capacity (Γ). The apparent porosity presented herein refers to the open porosity, which increased with the blending traction of RM but decreased with sintering temperature. According to Figure S2, the content of loss on ignition (LOI) increased with RM ratio, that is, the apparent porosity would increase when the combustible materials were removed. Since the LOI content of KRRM was higher than that of USRM, the porosity of the KRRM-based ceramsites was greater than that of USRM-based ones. Notably, the porosity of the KRRM-based and USRM-based ceramsites fired at high temperatures (T > 900 °C) varied distinctively. Since the USRM-based ceramsites did not undergo phase transformation, the alkali flux, i.e., Na_2O and CaO, vitrified and filled the pores to minimize the surface energy, which caused the porosity to decline (Cultrone et al., 2004). In contrast, the porosity of the KRRM-based ceramsites fired at T > 900 °C increased markedly and showed a high correlation with the content of new phases, *i.e.* plagioclases, nepheline, and gehlenite (will show later). Obviously, phase transition shrunken the crystal structure and thus porosity (Nowok et al., 1990).

The mechanical strength of ceramsites was evaluated by compression between two steel plates, resembling the point-load test. When 33.2% and 64.5% of the specimen were broken into 2 pieces and 3 pieces (Figure S5), individually, it suggested that the failure was originated from the tensile fracture of the flaws in the middle of the specimen (Hiramatsu and Oka, 1966; Wong and Einstein, 2009). Ceramsites are brittle materials that are porous and populated with flaws, such as defects, dislocation, and discontinuations (Li et al., 2000). The failure of brittle materials varied with shape, size, maximal tensile stress, orientation, and population of the flaws, which can be described by the Weibull distribution (Freiman and Mecholsky, 2012). Figure S6 and Figure S7 present the linearized Weibull distribution of the KRRM-based and USRM-based ceramsites, respectively; Table S4 and Table S5 summarize the corresponding parameters obtained. The probability of failure could be well described by the Weibull distribution since the values of correlation coefficient (r^2) were mostly greater than 0.90. The results confirmed that the ceramsites fractured from the flaw of the porous ceramic body as a brittle material. The variation of the mean tensile stress upon firing temperature is depicted in Fig. 5. Generally, the mean tensile stress decreased with the fraction of RM and increased with sintering temperature. Since no phase transformation occurred in the USRM-based ceramsites,

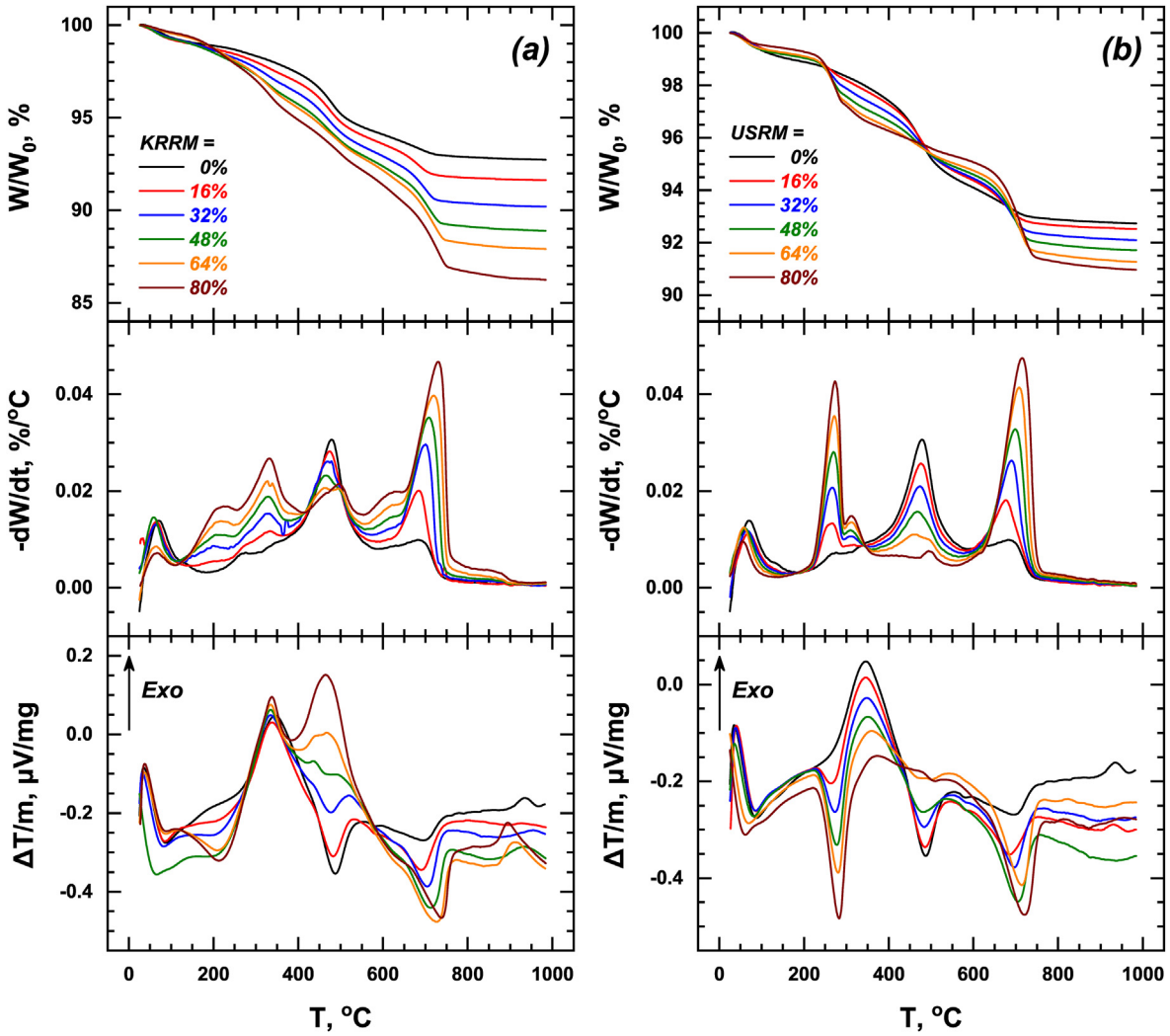

Fig. 3. Thermal analysis of (a) KRRM-based and (b) USRM-based green body. (KRRM + OCHR = 80 wt%, BENT = 20 wt%; ramping rate = 20 °C min^{-1}, purging gas = 50 mL-air min^{-1}). (For interpretation of the references to color in this figure legend, the reader is referred to the Web version of this article.)

the variations of the mean tensile stress as a function of USRM fraction at different firing temperature are parallel to each other. In contrast, the mean tensile stress of KRRM-based ceramsites fired at T > 900 °C decreased markedly when a phase transformation occurred. The transition from plagioclases to nepheline, from nepheline to gehlentie has been reported to promote the micro-cracks through closed pore opening mechanism and reaction-induced fracturing due to volume changes (Jamtveit et al., 2009; Nowok et al., 1990; Upadhyay, 2012).

We tested the phosphate adsorption capacity of the ceramsites at pH 6.8 with the initial phosphate concentration of 75 mg-P L^{-1}, as shown in Fig. 5. For the KRRM-based ceramsites fired at 700 °C, the adsorption capacity was around 0.5 mg-P g^{-1} regardless of the fraction of KRRM. As the sintering temperature increased, the adsorption capacity of the KRRM-based ceramsites declined dramatically except for the ones with phase transitions, which is attributable to the enhanced affinity of the new phases toward phosphate and increased porosity. On the other hand, the adsorption capacity of the USRM-based ceramsite increased with the fraction of USRM and decreased with the sintering temperature, indicating the adsorptive behavior was solely affected by the porosity and surface area reduction.

3.3. Correlation analysis

Table S6 shows results of the analysis of correlation among adsorption capacity and porosity and maximal stress of USRM-based ceramsites at the significant level of p-values < 0.01. Porosity showed a strong negative correlation with the maximal stress (|Pearson's | > 0.8), and a medium positive correlation with the adsorption capacity (0.4 < |Pearson's| < 0.8). A medium negative correlation between maximal stress and adsorption capacity was also observed. The correlations were reasonable as no phase transition was involved in the USRM-based ceramsites; the firing process minimized the porosity and flaw population, which enhanced the mechanical strength, but in turn decreased the adsorption capacity as the surface area was decreased.

Table S7 summarizes the correlation analysis of the KRRM-based ceramsites, including the ones without and with phase transition. For all KRRM-based ceramsites, the maximal stress and porosity showed high negative correlation with strong significance ($p < 0.01$), confirming the close relationship between porosity and the population of flaws and cracks. The phosphate adsorption capacity of the KRRM-based ceramsites without phase transition correlated positively with the porosity and the content of natrodavyne, but negatively with the content of quartz at significant

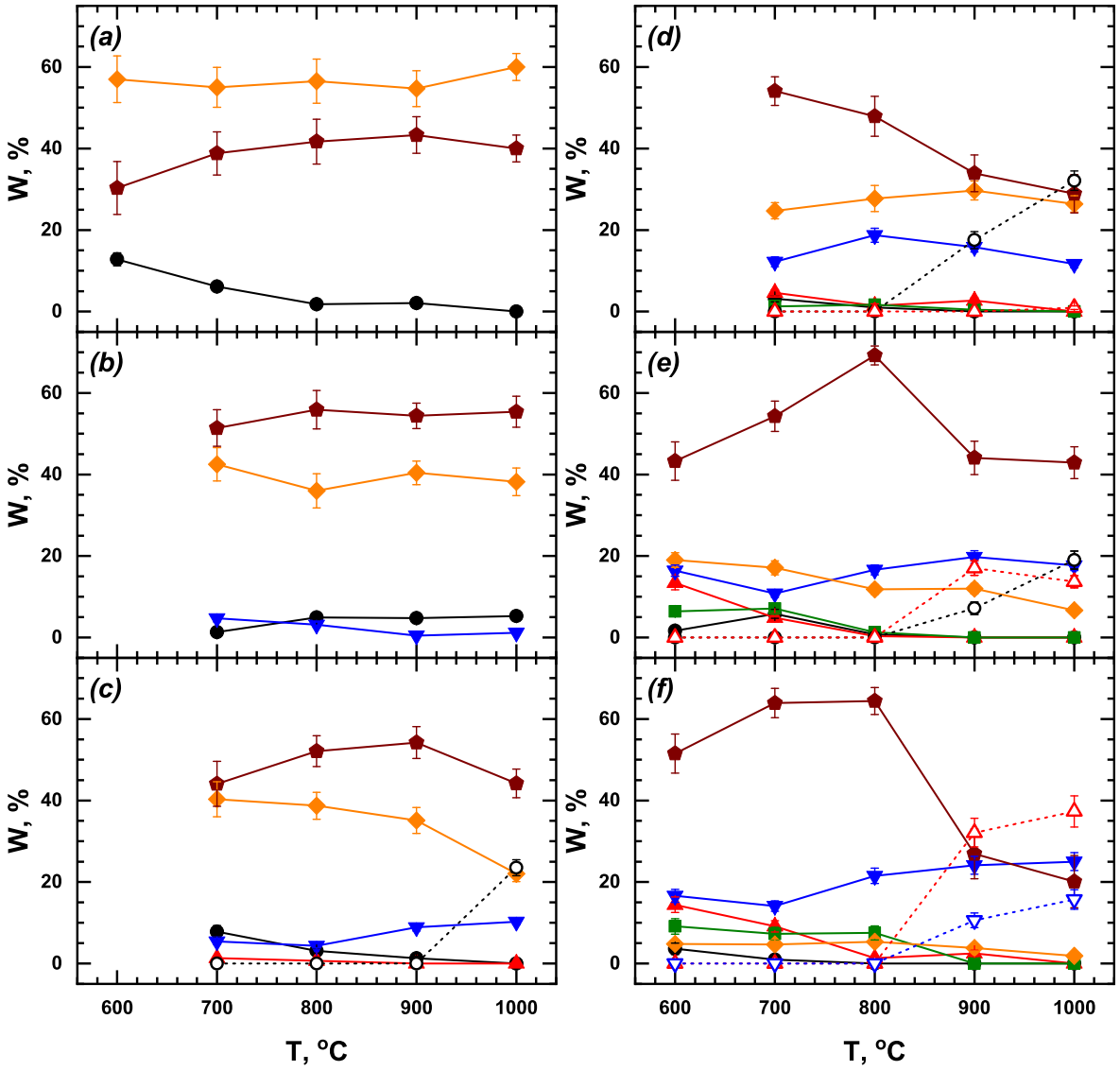

Fig. 4. Quantitative X-ray diffraction analysis of KRRM-based ceramsites consisting (a) 0, (b) 16, (c) 32, (d) 48 (e) 64 and (d) 80 wt% KRRM. Legends: ●: bentonite, ▲: calcite, ▼: hematite, ■: natrodavyne, ◆: quartz, ⬟: amorphous, ○: plagioclases, △: nepheline, ▽: gehlenite (Refer to Table 1 for diffraction standards.).

level of $p < 0.01$. Results suggested that porosity dominated the phosphate adsorption capacity while natrodavyne could be the major phase responsible for phosphate adsorption. In contrast, the correlation between the porosity and phosphate adsorption capacity of the KRRM-based ceramsites with phase transition was not statistically significant ($p > 0.05$). Instead, the phosphate adsorption capacity was highly correlated with the fraction of the new phases, *i.e.* plagioclases, ghelenite and nepheline, at significant level (Pearson's $r > 0.8$ and $p < 0.01$). Furthermore, the phosphate adsorption capacity correlated negatively with plagioclases but positively with ghelenite and nepheline. This outcome revealed that the phosphate adsorption capacity of the KRRM-based ceramsites with phase transition was dependent on the fraction of the new phases, specifically, ghelenite and nepheline.

3.4. Optimizing the granulation process

As revealed by above correlation analysis, the phosphate adsorption capacity was negatively correlated to the mechanical strength of the ceramsites. For field applications of ceramsites in phosphate control at fixed bed or construction wetland systems, it is necessary to maintain both high mechanical strength and phosphate adsorption capacity. Eq. (6) was used to determine the optimal condition for KRRM-based and USRM-based ceramsite.

$$E_i = \left(\frac{\Gamma_i}{\Gamma_{avg}}\right) \times \left(\frac{\sigma_i}{\sigma_{avg}}\right) \tag{6b}$$

where E_i, Γ_i and σ_i are the evaluation score, adsorption capacity (mg-P-g^{-1}), and mean tensile stress (MPa) of the *i*th specimen, respectively. Γ_{avg} and σ_{avg} are the average adsorption capacity (mg-P-g^{-1}) and tensile stress (MPa) of all specimen of the KRRM-based and USRM-based ceramsites tested. Fig. 6a and b presents the *E* value of the KRRM-based and USRM-based ceramsites, respectively. For the KRRM-based ceramsite, the optimal condition was at $E = 2.45$ (or $\Gamma_i/\Gamma_{avg} = 2.78$ and $\sigma_i/\sigma_{avg} = 0.88$), the one made with 64 wt% of KRRM at 1000 °C ($KR_{64\text{-}1000}$), On the contrary, the *E* value of the USRM-based ceramsites fired at 700 °C was 1.5 regardless of

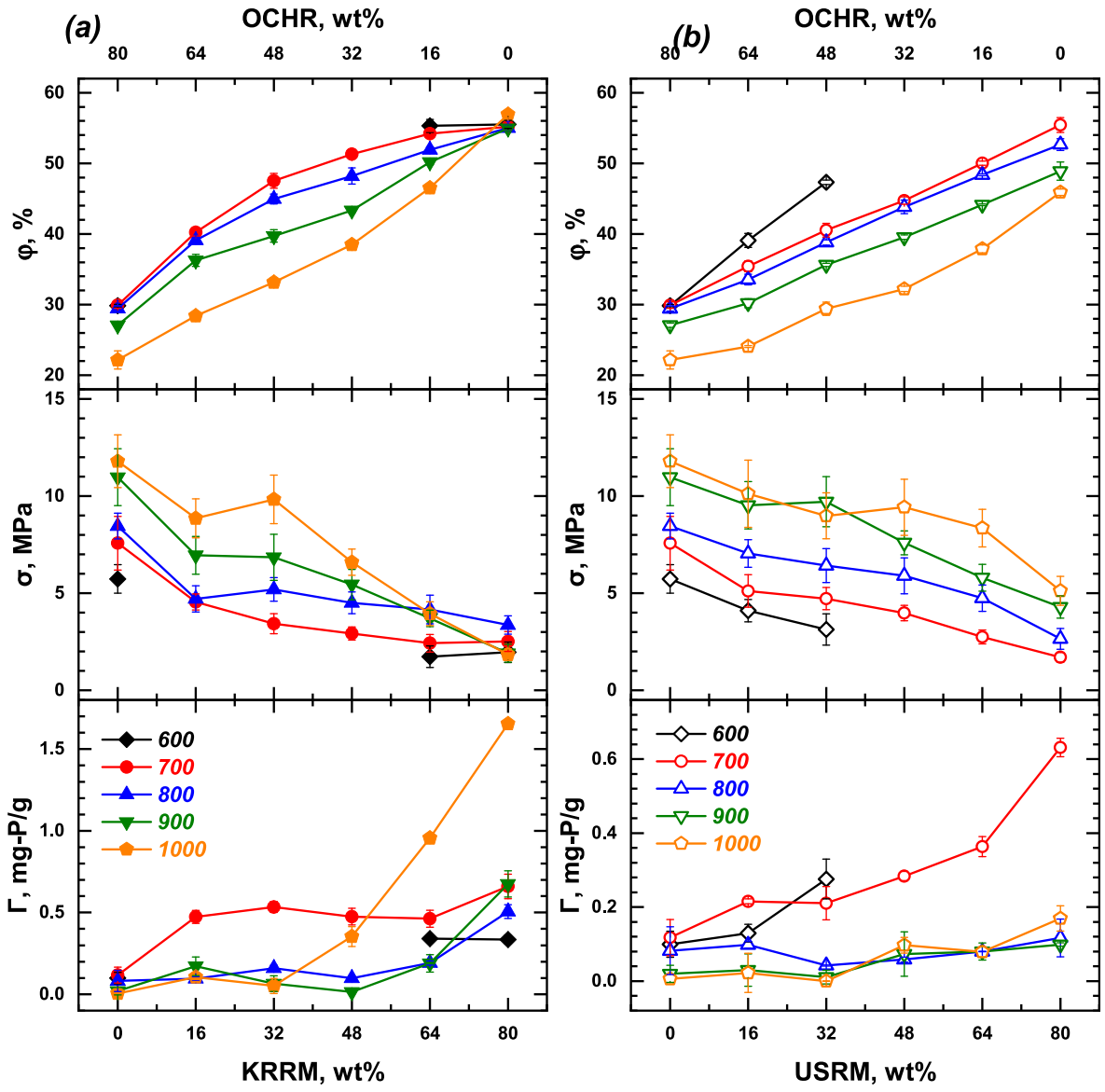

Fig. 5. Porosity (ϕ), maximal tensile stress (σ) and adsorption capacity (Γ) of (a) KRRM-based and (b) USRM-based ceramsites.

USRM wt%. Therefore, the optimal condition selected was at E of 1.32 for the ceramites prepared with 48 wt% of USRM and at 700 °C ($US_{48\text{-}700}$), which had the least trade-off between the mechanical strength ($\Gamma_i/\Gamma_{avg} = 2.2$) and the phosphate adsorption capacity ($\sigma_i/\sigma_{avg} = 0.6$).

The evaluation of both ceramsites based on the bulk density-tensile stress and porosity-tensile stress were also conducted (S4, Supporting Information). Figure S8 presents the process evaluation based on the bulk density and tensile stress, as suggested by Cheng et al. (2018) and Zou et al. (2009). Apparently, it is not an appropriate mean to evaluate ceramsites since the method would recommend optimal ceramsites be prepared by sintering at 1000 °C without RMs, under which condition there would be no phosphate adsorption capacity (Fig. 5). The process evaluation based on porosity and tensile stress is with flaws (Figure S9). The optimized ceramsites, in terms of physical properties, namely, bulk density-tensile stress or porosity-tensile stress, were ones prepared with 32 wt% of KRRM at 1000 °C and 32 wt% of USRM at 900 °C. However, the phosphate adsorption capacity of the above ceramsites were relatively poor (Fig. 5). Thus, the process optimization for ceramsites according to bulk density-tensile stress or porosity-tensile stress should not be recommended; instead, it should be optimized based on the adsorption capacity and mechanical strength directly.

3.5. Mechanism of phosphate adsorption by the optimized ceramsites

The phosphate adsorption characteristics on the optimized KRRM-based ceramsites (64 wt% of KRRM at 1000 °C, $KR_{64\text{-}1000}$) and USRM-based ceramsites (48 wt% of USRM at 700 °C, $US_{48\text{-}700}$) were investigated in details as to evaluate their potential uses as a substrate of constructed wetlands. Considering that the pH value of conventional constructed wetlands is mostly neutral, i.e., 6.2–7.8 (Valipour and Ahn, 2016), the adsorption experiments were investigated at pH 6.8 with an emphasis on the kinetics and equilibrium adsorption isotherms of phosphate adsorption on ceramites. Nevertheless, both KRRM-based and USRM-based ceramsites were expected to show greater adsorption capacity at lower pH ~4 (Huang et al., 2009; Lin et al., 2020). Furthermore, the reusability

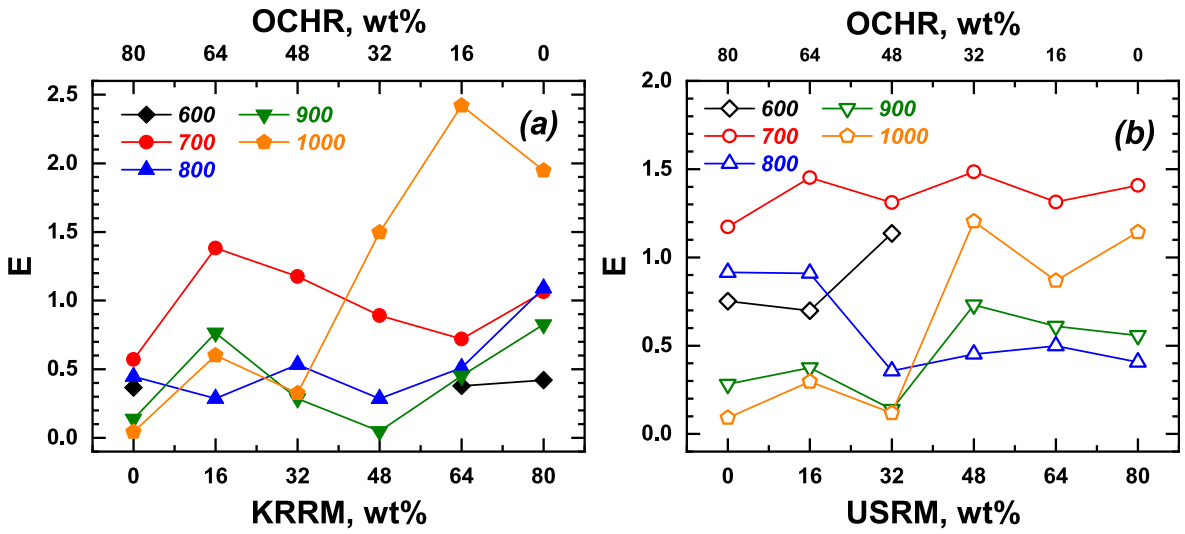

Fig. 6. Evaluation of (a) KRRM-based and (b) USRM-based ceramsites according to Eq. (6).

test of the ceramsites was not done as the substrate should last years to minimize frequent replacement or regeneration (Shilton et al., 2006). Fig. 7a and b shows the phosphate uptake by $KR_{64\text{-}1000}$ and $US_{48\text{-}700}$ ceramsites at 20 °C and various initial concentrations. Clearly, the adsorption of phosphate on of both ceramsites was rather slow, especially, the ones with greater initial concentrations, which had not reached equilibrium in one week (168 h).

The adsorption kinetics of KRRM-based and USRM-based was fitted by the pseudo-second order model (Tran et al., 2017):

$$\frac{d\Gamma}{dt} = k_2(\Gamma_e - \Gamma)^2 \tag{7a}$$

or

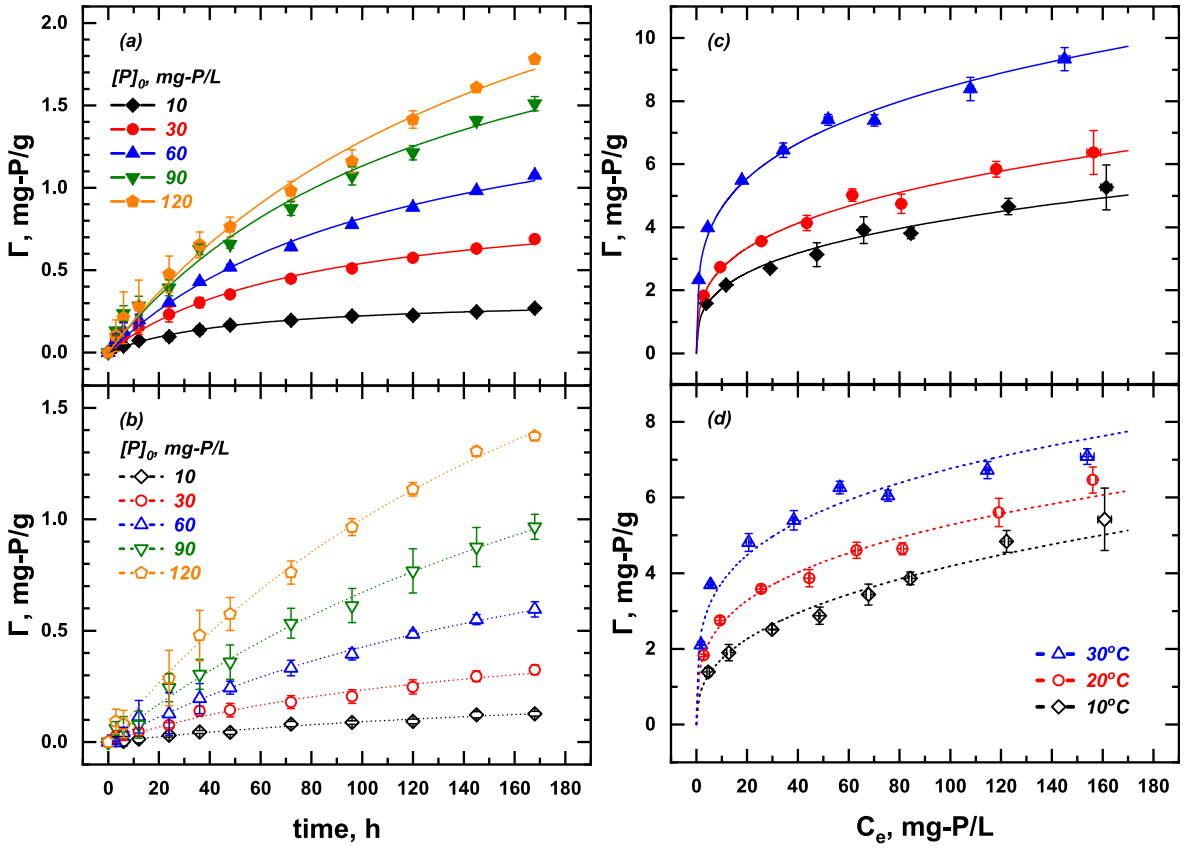

Fig. 7. Phosphorus adsorption using optimized KRRM-based ceramsites ($KR_{64\text{-}1000}$) and USRM-based ceramsites ($US_{48\text{-}700}$). Kinetic of phosphate uptake by (a) $KR_{64\text{-}1000}$ and (b) US48-700 (pH = 6.8 ± 0.3, I = 10 mM NaCl, X = 20 g/L); isotherms of ground (a) $KR_{64\text{-}1000}$ and (b) US48-700 at various temperature (pH = 6.8 ± 0.3, I = 10 mM NaCl, X = 4 g/L, equilibrium time = 4 d).

$$\Gamma = \frac{k_2 t \Gamma_e^2}{k_2 t \Gamma_e + 1} \quad (7b)$$

where Γ (mg-P/g) is the adsorption capacity at time t (h); Γ_e (mg-P/g) is the equilibrium adsorption capacity; k_2 is the pseudo-second order rate constant (g/(mg-P•h)). The fitting results are summarized in Table S8. Based on the high R^2 values, the pseudo-second order model was sufficient to describe the kinetics of phosphate adsorption. Notably, $KR_{64\text{-}1000}$ appeared to be more effective in the removal of phosphorus than $US_{48\text{-}700}$ in terms of both equilibrium adsorption capacity and rate constant. As the adsorption of phosphate on ceramsites was slow, the adsorption isotherm was established using ground ceramsites (finer than 250 μm or passing 60 mesh) instead of intact granules. As can be seen in Fig. 7c and d, the adsorption capacity of phosphate on both ground $KR_{64\text{-}1000}$ and $US_{48\text{-}700}$ increased with equilibrium phosphate concentration and temperature. The equilibrium phosphate adsorption can be well described by the Freudlich isotherm:

$$\Gamma = K_F C_e^{1/n} \quad (8)$$

where Γ is adsorption capacity (mg-P/g), K_F and n are constants with n being greater than 1. Table S9, summarizes the parameters of Freundlich. Results show that both K_F and n increased with temperature, indicating the variation in surface heterogeneity and equilibrium state between red mud surface and phosphate. It is clear that the phosphorus adsorption capacity of $KR_{64\text{-}1000}$ was superior to $US_{48\text{-}1000}$, however, the surface area and pore volume of the former actually were smaller than the latter. Based on the N_2 adsorption-desorption hysteresis (Figure S10), the specific surface area (SSA) and pore volume (V_{pore}) of $KR_{32\text{-}1000}$ were 2.3 m^2/g and 7.5 × 10^{-3} cm^3/g, according to BET and BJH models, respectively. The small SSA and V_{pore} was attributed to the vitrification and phase transformation of $KR_{64\text{-}1000}$ during the sintering process, which eliminated the microstructure to minimize the surface energy (Lin et al., 2020). In contrast, the SSA and V_{pore} of $US_{48\text{-}900}$ were retained at 24.2 m^2/g and 0.099 cm^3/g, individually, because no prominent phase transformation occurred. The pore size distribution suggested that most of pores of $US_{48\text{-}900}$ were mesoporous (pore diameter of 2–50 nm), which is beneficial for phosphate adsorption due to much accessible red mud surface (Hyok Ri et al., 2021; Shi et al., 2020; Zhang et al., 2021). Furthermore, the phosphate uptake by $KR_{64\text{-}1000}$ did not occur in monolayer fashion, rather phosphate adsorption occurred in 90 layers, based on the total adsorption density of 89.8 μmol/m^2 at 20 °C with respect to the theoretical monolayer phosphate coverage density of 5.8 μmol/m^2 (Lin et al., 2020). In other words, the phosphate was immobilized *via* surface precipitation enabled by the dissolution of the calcium-based and aluminum-based minerals, e.g., plagioclases, nepheline, and gehlenite (Lin et al., 2020). On the contrary, the surface coverage of $US_{48\text{-}900}$ (8.0 μmol/m^2) was of the same order of magnitude as the theoretical monolayer coverage, indicating that the surface precipitation was not prominent. The above observation was consistent with the major crystalline phase of $US_{48\text{-}900}$, hematite, which has a low solubility at neutral pH. Lastly, the phosphate adsorption capability of the optimized red mud-based ceramsites was comparable with that of other industrial waste-derived adsorbents. Table S10 reveals that the adsorption capacity of the optimized KRRM-based and US-based ceramsites was comparable to other adsorbents originated from waste residues. In summary, the red mud-based ceramsites will have great potential for application in phosphate removal from water.

4. Conclusion

The ceramsites based on Korean red mud (KRRM) and American red mud (USRM) were prepared with the addition of OCHR and BENT in the sintering temperature range of 600–1000 °C for phosphate immobilization. The characteristics of the ceramsites, including porosity, maximal tensile stress, and phosphate adsorption capacity varied with the composition of raw materials and the firing temperature. Since KRRM had higher content of alkali flux (Na_2O and CaO), the crystallization of plagioclases, nepheline, and gehlenite was observed in the KRRM-based ceramsites, which increased both the porosity and phosphate adsorption capacity. The phosphate adsorption capacity of the ceramsites without phase transformation showed a positive correlation with porosity due to the reduction of surface area. The failure pattern of ceramsites agreed with brittle materials, which was governed by flaw population and could be described by the Weibull distribution model. Hence, the optimal formulation for the synthesis of ceramsites could be established by simultaneous evaluation of the phosphate adsorption capacity and maximal tensile stress. The kinetics and equilibrium of phosphate adsorption of the optimized ceramsites, namely, $KR_{64\text{-}1000}$ and $US_{48\text{-}700}$ were studied. Results indicated that pseudo second-order reaction rate law and Freundlich adsorption isotherm better described the mode of phosphate adsorption on ceramites. The optimized ceramsites will be an idea substrate for constructed wetlands, primarily for the elimination of micronutrients such as phosphate. Further study on the biocompatibility and the effect of biofouling and competing ions on the adsorptive removal of phosphorus is highly desirable.

Credit statement

Jui-Yen Lin: Writing – original draft, Data curation; Formal analysis, Investigation. Dan Li: Resources. Minsoo Kim: Resources. Inyu Lee: Resources. Hyunook Kim: Project administration, Visualization, Validation, review and editing, Chin-Pao Huang: Conceptualization, Supervision, Visualization, Validation, Writing – review & editing

Declaration of competing interest

The authors declare that they have no known competing financial interests or personal relationships that could have appeared to influence the work reported in this paper.

Acknowledgements

This research was performed under the support from WENi, Seoul, South Korea. Hyunook Kim and Minsoo Kim were supported by the Basic Study and Interdisciplinary R&D Foundation Fund of the University of Seoul (2020). The authors would like to thank Ministry of Science and Technology, Taiwan for financial supports to Jui-Yen Lin under contract No. MOST-107-2917-I-006-013. The assistance of Mr. Valdez and Ms. Garvizu is greatly appreciated.

Appendix A. Supplementary data

Supplementary data to this article can be found online at https://doi.org/10.1016/j.chemosphere.2021.130239.

References

ASTM, 2016. Practice for Calculating Areas, Volume, and Linear Change of Refractory Shapes (No. C1407- 98(2016)). ASTM International, West Conshohocken, PA.
ASTM, 2015. Test Methods for Apparent Porosity, Water Absorption, Apparent

Specific Gravity, and Bulk Density of Burned Refractory Brick and Shapes by Boiling Water (No. C20- 00(2015)). ASTM International, West Conshohocken, PA.
ASTM, 2012. Practice for Maintaining Constant Relative Humidity by Means of Aqueous Solutions (No. E104- 02 (2012)). ASTM International, West Conshohocken, PA.
Bhatnagar, A., Vilar, V.J.P., Botelho, C.M.S., Boaventura, R.A.R., 2011. A review of the use of red mud as adsorbent for the removal of toxic pollutants from water and wastewater. Environ. Technol. 32, 231–249.
Buhl, J.C., 1991. Synthesis and characterization of the basic and non-basic members of the cancrinite-natrodavyne family. Thermochim. Acta 178, 19–31.
Cheng, G., Li, Q., Su, Z., Sheng, S., Fu, J., 2018. Preparation, optimization, and application of sustainable ceramsite substrate from coal fly ash/waterworks sludge/oyster shell for phosphorus immobilization in constructed wetlands. J. Clean. Prod. 175, 572–581.
Cultrone, G., Sebastián, E., Elert, K., de la Torre, M.J., Cazalla, O., Rodriguez–Navarro, C., 2004. Influence of mineralogy and firing temperature on the porosity of bricks. J. Eur. Ceram. Soc. 24, 547–564.
Doebelin, N., Kleeberg, R., 2015. Profex: a graphical user interface for the Rietveld refinement program BGMN. J. Appl. Crystallogr. 48, 1573–1580.
Freiman, S.W., Mecholsky, J.J., 2012. The Fracture of Brittle Materials: Testing and Analysis. John Wiley & Sons, Hoboken, N.J.
Ge, J., Yoon, S., Choi, N., 2018. Application of fly ash as an adsorbent for removal of air and water pollutants. Appl. Sci. 8, 1116.
Gérard, F., 2016. Clay minerals, iron/aluminum oxides, and their contribution to phosphate sorption in soils — a myth revisited. Geoderma 262, 213–226.
Girgis, B.S., El-Barawy, K.A., Felix, N.S., 1987. Dehydration kinetics of some smectites: a thermogravimetric study. Thermochim. Acta 111, 9–19.
He, H., Yue, Q., Qi, Y., Gao, B., Zhao, Y., Yu, H., Li, J., Li, Q., Wang, Y., 2012. The effect of incorporation of red mud on the properties of clay ceramic bodies. Appl. Clay Sci. 70, 67–73.
Hind, A.R., Bhargava, S.K., Grocott, S.C., 1999. The surface chemistry of Bayer process solids: a review. Colloids Surf. Physicochem. Eng. Asp. 146, 359–374.
Hiramatsu, Y., Oka, Y., 1966. Determination of the tensile strength of rock by a compression test of an irregular test piece. Int. J. Rock Mech. Min. Sci. Geomech. Abstr. 3, 89–90.
Hu, Y., Liang, S., Yang, J., Chen, Y., Ye, N., Ke, Y., Tao, S., Xiao, K., Hu, J., Hou, H., Fan, W., Zhu, S., Zhang, Y., Xiao, B., 2019. Role of Fe species in geopolymer synthesized from alkali-thermal pretreated Fe-rich Bayer red mud. Construct. Build. Mater. 200, 398–407.
Huang, W., Zhang, Y., Li, D., 2017. Adsorptive removal of phosphate from water using mesoporous materials: a review. J. Environ. Manag. 193, 470–482.
Huang, X., Foster, G.D., Honeychuck, R.V., Schreifels, J.A., 2009. The maximum of phosphate adsorption at pH 4.0: why it appears on aluminum oxides but not on iron oxides. Langmuir 25, 4450–4461.
Hyok Ri, S., Bi, F., Guan, A., Zhang, X., 2021. Manganese-cerium composite oxide pyrolyzed from metal organic framework supporting palladium nanoparticles for efficient toluene oxidation. J. Colloid Interface Sci. 586, 836–846.
International Aluminium Institute, 2015. Bauxite Residue Management: Best Practice.
Jamtveit, B., Putnis, C.V., Malthe-Sørenssen, A., 2009. Reaction induced fracturing during replacement processes. Contrib. Mineral. Petrol. 157, 127–133.
Jellali, S., Wahab, M.A., Hassine, R.B., Hamzaoui, A.H., Bousselmi, L., 2011. Adsorption characteristics of phosphorus from aqueous solutions onto phosphate mine wastes. Chem. Eng. J. 169, 157–165.
Johannes, W., Koepke, J., Behrens, H., 1994. Partial melting reactions of plagioclases and plagioclase-bearing systems. In: Parsons, I. (Ed.), Feldspars and Their Reactions. Springer Netherlands, Dordrecht, pp. 161–194.
Kloprogge, J.T., Ruan, H.D., Frost, R.L., 2002. Thermal decomposition of bauxite minerals: infrared emission spectroscopy of gibbsite, boehmite and diaspore. J. Mater. Sci. 37, 1121–1129.
Li, M., Liu, J., Xu, Y., Qian, G., 2016. Phosphate adsorption on metal oxides and metal hydroxides: a comparative review. Environ. Rev. 24, 319–332.
Li, Y., Wu, Dongfang, Zhang, J., Chang, L., Wu, Dihua, Fang, Z., Shi, Y., 2000. Measurement and statistics of single pellet mechanical strength of differently shaped catalysts. Powder Technol. 113, 176–184.
Lin, J.-Y., Kim, M., Li, D., Kim, H., Huang, C., 2020. The removal of phosphate by thermally treated red mud from water: the effect of surface chemistry on phosphate immobilization. Chemosphere 247, 125867.
Liu, M., Xu, G., Li, G., 2017. Effect of the ratio of components on the characteristics of lightweight aggregate made from sewage sludge and river sediment. Process Saf. Environ. Protect. 105, 109–116.
Liu, Y., Naidu, R., Ming, H., 2013. Surface electrochemical properties of red mud (bauxite residue): zeta potential and surface charge density. J. Colloid Interface Sci. 394, 451–457.
Liu, Y., Naidu, R., Ming, H., 2011. Red mud as an amendment for pollutants in solid and liquid phases. Geoderma 163, 1–12.
Lu, M., Xia, G.-H., Liao, R.-H., Zhao, X.-D., 2013. Preparation and modification of porous lightweight ceramsite and its performance investigation. Desalination Water Treat 51, 4651–4657.
Nowok, J.W., Benson, S.A., Jones, M.L., Kalmanovitch, D.P., 1990. Sintering behaviour and strength development in various coal ashes. Fuel 69, 1020–1028.
Pejchal, V., Žagar, G., Charvet, R., Dénéréaz, C., Mortensen, A., 2017. Compression testing spherical particles for strength: theory of the meridian crack test and implementation for microscopic fused quartz. J. Mech. Phys. Solid. 99, 70–92.
Plante, A.F., Fernández, J.M., Leifeld, J., 2009. Application of thermal analysis techniques in soil science. Geoderma 153, 1–10.
Provenzano, M.R., Senesi, N., 1999. Thermal properties of standard and reference humic substances by differential scanning calorimetry. J. Therm. Anal. Calorim. 57, 517–526.
Radha, A.V., Forbes, T.Z., Killian, C.E., Gilbert, P.U.P.A., Navrotsky, A., 2010. Transformation and crystallization energetics of synthetic and biogenic amorphous calcium carbonate. Proc. Natl. Acad. Sci. U.S.A. 107, 16438–16443.
Shi, X., Zhang, X., Bi, F., Zheng, Z., Sheng, L., Xu, J., Wang, Z., Yang, Y., 2020. Effective toluene adsorption over defective UiO-66-NH_2: an experimental and computational exploration. J. Mol. Liq. 316, 113812.
Shilton, A.N., Elmetri, I., Drizo, A., Pratt, S., Haverkamp, R.G., Bilby, S.C., 2006. Phosphorus removal by an 'active' slag filter–a decade of full scale experience. Water Res. 40, 113–118.
Stanković, N., Logar, M., Luković, J., Pantić, J., Miljević, M., Babić, B., Radosavljević-Mihajlović, A., 2011. Characterization of bentonite clay from "Greda" deposit. Process. Appl. Ceram. 5, 97–101.
Tor, A., Danaoglu, N., Arslan, G., Cengeloglu, Y., 2009. Removal of fluoride from water by using granular red mud: batch and column studies. J. Hazard Mater. 164, 271–278.
Tran, H.N., You, S.-J., Hosseini-Bandegharaei, A., Chao, H.-P., 2017. Mistakes and inconsistencies regarding adsorption of contaminants from aqueous solutions: a critical review. Water Res. 120, 88–116.
Upadhyay, D., 2012. Alteration of plagioclase to nepheline in the Khariar alkaline complex, SE India: constraints on metasomatic replacement reaction mechanisms. Lithos 155, 19–29.
Valipour, A., Ahn, Y.-H., 2016. Constructed wetlands as sustainable ecotechnologies in decentralization practices: a review. Environ. Sci. Pollut. Res. 23, 180–197.
Wei, Y.-L., Cheng, S.-H., Ou, K.-T., Kuo, P.-J., Chung, T.-H., Xie, X.-Q., 2017. Effect of calcium compounds on lightweight aggregates prepared by firing a mixture of coal fly ash and waste glass. Ceram. Int. 43, 15573–15579.
Wei, Y.-L., Ko, G.-W., 2017. Recycling steel wastewater sludges as raw materials for preparing lightweight aggregates. J. Clean. Prod. 165, 905–916.
Wolters, F., Emmerich, K., 2007. Thermal reactions of smectites—relation of dehydroxylation temperature to octahedral structure. Thermochim. Acta 462, 80–88.
Wong, L.N.Y., Einstein, H.H., 2009. Systematic evaluation of cracking behavior in specimens containing single flaws under uniaxial compression. Int. J. Rock Mech. Min. Sci. 46, 239–249.
Wu, J., Xu, D., He, F., He, J., Wu, Z., 2015. Comprehensive evaluation of substrates in vertical-flow constructed wetlands for domestic wastewater treatment. Water Pract. Technol. 10, 625–632.
Yang, ZhengHong, Song, WenJuan, Yang, JianHui, Deng, Lei, Cao, Zhen, Shi, MeiLun, 2013. High-strength ceramsite made with sludge and low-quality fly ash. J. Mater. Civ. Eng. 25, 851–856.
Yasipourtehrani, S., Strezov, V., Evans, T., 2019. Investigation of phosphate removal capability of blast furnace slag in wastewater treatment. Sci. Rep. 9, 7498.
Ye, J., Cong, X., Zhang, P., Hoffmann, E., Zeng, G., Wu, Y., Zhang, H., Fang, W., 2015. Preparation of a new granular acid-activated neutralized red mud and evaluation of its performance for phosphate adsorption. ACS Sustain. Chem. Eng. 3, 3324–3331.
Yue, Q., Zhao, Y., Li, Q., Li, W., Gao, B., Han, S., Qi, Y., Yu, H., 2010. Research on the characteristics of red mud granular adsorbents (RMGA) for phosphate removal. J. Hazard Mater. 176, 741–748.
Zhang, Xiaodong, Chen, J., Jiang, S., Zhang, Xialu, Bi, F., Yang, Y., Wang, Y., Wang, Z., 2021. Enhanced photocatalytic degradation of gaseous toluene and liquidus tetracycline by anatase/rutile titanium dioxide with heterophase junction derived from materials of Institut Lavoisier-125(Ti): degradation pathway and mechanism studies. J. Colloid Interface Sci. 588, 122–137.
Zhao, Y., Yue, Q., Li, Q., Gao, B., Han, S., Yu, H., 2010. The regeneration characteristics of various red mud granular adsorbents (RMGA) for phosphate removal using different desorption reagents. J. Hazard Mater. 182, 309–316.
Zhao, Y., Yue, Q., Li, Q., Xu, X., Yang, Z., Wang, X., Gao, B., Yu, H., 2012a. Characterization of red mud granular adsorbent (RMGA) and its performance on phosphate removal from aqueous solution. Chem. Eng. J. 193–194, 161–168.
Zhao, Y., Yue, Q., Li, Qian, Li, Qiuju, Gao, B., Han, S., Yu, H., 2012b. Influence of sintering temperature on orthophosphate and pyrophosphate removal behaviors of red mud granular adsorbents (RMGA). Colloids Surf. Physicochem. Eng. Asp. 394, 1–7.
Zhou, X., Liu, D., Bu, H., Deng, L., Liu, H., Yuan, P., Du, P., Song, H., 2018. XRD-based quantitative analysis of clay minerals using reference intensity ratios, mineral intensity factors, Rietveld, and full pattern summation methods: a critical review. Solid Earth Sci 3, 16–29.
Zhu, C., Luan, Z., Wang, Y., Shan, X., 2007. Removal of cadmium from aqueous solutions by adsorption on granular red mud (GRM). Separ. Purif. Technol. 57, 161–169.
Zou, J.L., Xu, G.R., Li, G.B., 2009. Ceramsite obtained from water and wastewater sludge and its characteristics affected by Fe_2O_3, CaO, and MgO. J. Hazard Mater. 165, 995–1001.